Orocline and syntaxes formation during subduction and collision

Flora Bajolet, Anne Replumaz, Romain Lainé

TECTONICS, VOL. 32, 1529–1546, doi:10.1002/tect.20087, 2013

Orocline and syntaxes formation during subduction and collision

Flora Bajolet,[1,2] Anne Replumaz,[3,4] and Romain Lainé[3,4]

Received 23 December 2012; revised 7 September 2013; accepted 16 September 2013; published 21 October 2013.

[1] The present work investigates the formation of curved ranges and syntaxes with scaled laboratory experiments. We simulated subduction and collision processes comparable to India-Asia configuration involving a continental upper plate and a subducting plate composed of an oceanic lithosphere and a continental indenter. The experiments reveal that the shape of the mountain range (concave, straight, or convex) and the development of syntaxes are controlled by the subduction interface, the buoyancy number (F_b) of the upper plate (i.e., thickness and viscosity), and the boundary conditions. Four end-members regimes of indentation can be defined depending on the range shape and dynamics of the upper plate. The curvature of the range is convex toward the subducting plate with syntaxes for a weak subduction fault and concave without syntaxes for a strong subduction fault. Convex curvature and syntaxes form by overthrusting of upper plate material on the subducting plate, which is faster at the center than at the extremities. They are associated with a rather flat slab (underthrusting) during continental collision. Low-F_b experiments show less pronounced curvatures associated to thickening comparable to the early stages of the India-Asia collision. In contrast, a thick and weak upper plate (high F_b) leads to gravity collapse that increases the amplitude of the curvature and lateral escape, similar to the late evolution of the Himalaya-Tibet system. Important lateral decoupling on the sides of the indenter enhances the indentation and produces sharper syntaxes.

Citation: Bajolet, F., A. Replumaz, and R. Lainé (2013), Orocline and syntaxes formation during subduction and collision, *Tectonics*, *32*, 1529–1546, doi:10.1002/tect.20087.

1. Introduction

[2] One striking feature of mountain belts worldwide is the diversity of shapes they can adopt. Most of the mountain ranges show a curvature concave toward the overriding plate (e.g., Andes, Alps, and Bitlis) or straight (e.g., Pyrenees and Rockies Mountains). On the contrary, the Himalayas show an unusual shape convex toward the overriding plate. The overall geometry of the range is more complex, with a large penetration of India far north into the Asian continent and two curves in the trend of the range at both east and west extremities, named large-scale syntaxes (Figure 1). This penetration is accommodated by two north-south strike-slip faults: the Sagaing fault to the east and the Chaman fault to the west. India slid north, leaving behind the two lateral oceans subducting beneath Makran to the west and Sumatra to the east. The Tsangpo suture, which is the trace of the Tethys Ocean closed between India and Asia, follows the shape of the range (Figure 1). In detail, the suture shows two small-scale sharp curves around the Nanga Parbat to the west and around the Namche Barwa to the east named small-scale syntaxes. The curvature of the range generates oblique convergence and strain partitioning in the Asian upper plate, which has a fundamental influence on stress pattern and faulting [e.g., *Seeber and Pêcher*, 1998; *McCaffrey and Nabelek*, 1998; *Kapp and Guynn*, 2004; *Bonnardot et al*., 2008; *Mohadjer et al*., 2010]. However, the origin of the curvature of the Himalayan range and possible links with the subduction/collision processes remain poorly understood.

[3] The indentation process is driven by a vigorous advance of the Indian plate [*Molnar and Stock*, 2009]. Mantle tomography shows that pieces of the Indian lithosphere have subducted and that India is overriding its own continental slab [e.g., *van der Voo et al*., 1999; *Replumaz et al*., 2010b]. The Indian continental lithosphere has long been considered too buoyant to actively drive subduction, and external forcing, such as Indian Ocean ridge push or pull of neighboring slabs, has to be invoked [*Chemenda et al*., 2000; *Li et al*., 2008]. Recently, it has been shown that the continental lithosphere of India could not lead to a continuous subduction unless India is scraped off its upper crust and part of its lower crust [*Capitanio et al*., 2011]. This is the case for the Himalayan range, which grows up as a sedimentary wedge [e.g., *Malavieille*, 1984] by scraping of the Indian upper crust along the Main Himalayan Thrust [e.g., *Lavé and Avouac*, 2000]. The subduction process could also be facilitated by the eclogitization of the lower crust, becoming denser than the mantle, when it bent beneath the Himalaya range [e.g.,

[1]Laboratory of Experimental Tectonics, Università Roma TRE, Rome, Italy.
[2]Now at GET, Observatoire Midi-Pyrénées, Université de Toulouse, CNRS, IRD, Toulouse, France.
[3]University Grenoble Alpes, ISTerre, Grenoble, France.
[4]CNRS, ISTerre, Grenoble, France.

Corresponding author: F. Bajolet, GET-Géosciences Environnement Toulouse, Observatoire Midi-Pyrénées, Université de Toulouse, 14 avenue Edouard Belin, 31400 Toulouse, France. (flora.bajolet@get.obs-mip.fr)

0278-7407/13/10.1002/tect.20087

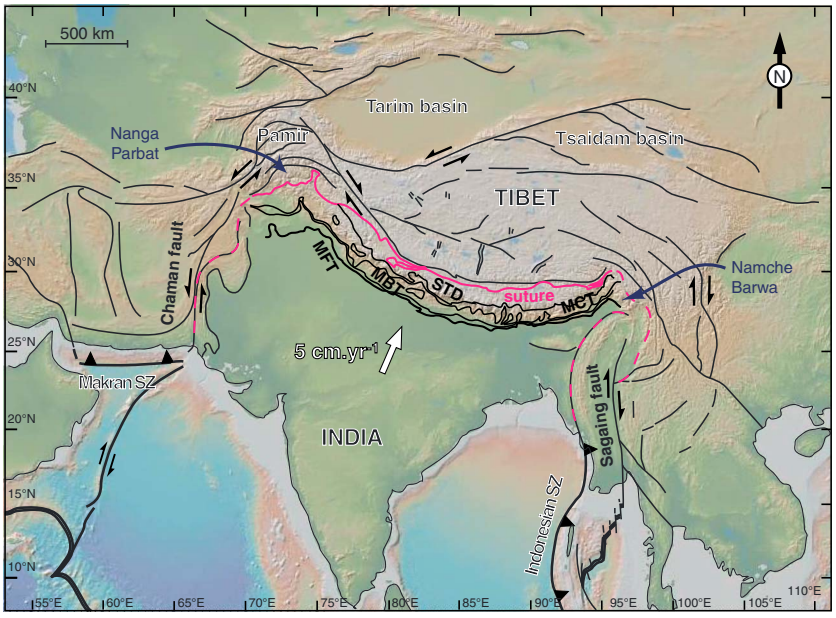

Figure 1. Map of the geodynamic context of India-Asia collision. Main faults are drawn in bold, and the suture between Indian and Asian plate is underlined in pink. STD: South Tibetan Detachment; MCT: Main Central Thrust; MBT: Main Boundary Thrust; MFT: Main Frontal Thrust; SZ: Subduction Zone.

Hetenyi et al., 2007]. But external forcing has still to be invoked to reproduce the high velocity of the India-Asia convergence, the trench advance, and the overriding of the Indian slab. The mantle drag exerted on the base of the lithosphere by a large-scale convective belt with an active upwelling component is likely the main cause for the ongoing indentation of the Indian plate into Eurasia [*Alvarez*, 2010; *Becker and Faccenna*, 2011]. The northward motion of India occurs at about 5 cm yr^{-1}, an almost constant rate since the beginning of the collision about 50 My ago [*Patriat and Achache*, 1984; *Molnar and Stock*, 2009].

[4] The curvature of the trench has been observed in subduction experiments where an oceanic plate subducts under its own weight. The trench curves toward the subducting plate if the slab retreats or is straight if steep subduction occurs [*Funiciello et al*., 2003; *Stegman et al*., 2010]. This is consistent with natural examples [*Lallemand et al*., 2005]. With a continental upper plate, the trench curves toward the subducting oceanic plate if an older thus denser part is introduced in the middle of the subducting plate, while an opposite curvature is obtained with the denser heterogeneity placed in the upper plate [*Capitanio et al*., 2011]. But very few studies explore orocline evolution in continental collision settings, and most models applied to India-Asia orogen do not include the influence of the subduction process [e.g., *England and Houseman*, 1986; *Copley*, 2012] or use a preshaped plate boundary with a convex curvature [e.g., *McCaffrey and Nabelek*, 1998; *Seeber and Pecher*, 1998; *Bonnardot et al*., 2008]. The indentation process has been previously simulated with a rigid, non-deformable indenter thus preventing any curvature but reproducing lateral escape and extrusion [*Tapponnier et al*., 1982; *Sokoutis et al*., 2000; *Cruden et al*., 2006; *Rosenberg et al*., 2007]. Strong but deformable plates indenting weaker ones have been used resulting in a straight or concave curvature, but without taking into account the subduction stage [e.g., *Keep*, 2000; *Sokoutis and Willingshofer*, 2011]. *Regard et al.* [2005] use a deformable subducting plate including lateral variations to explore the links between indentation and subduction dynamics. In that setup, the curvature of the oceanic slab (convex) opposes that of the continental one (concave). In this paper we present analog models performed to simulate in three dimensions, at the scale of the mantle-lithosphere system, the mechanics of the indentation process for a continental lithosphere. We test (1) which geometry and rheological parameters favor arcuate orogen and syntaxes formation, (2) what are the consequences on the topography and strain of both the orogenic front and the plateau, and (3) how they relate to the subduction/collision dynamics.

2. Model Setup and Experimental Procedure

2.1. Model Setup

[5] The model is composed of thin sheets of silicone putty (analog for lithospheres) lying on top of low-viscosity glucose syrup simulating the asthenospheric mantle. One silicone layer reproduces the overriding continental plate. The subducting plate is composed of a dense silicone layer representing the oceanic lithosphere (analog for the Tethys Ocean at the front) attached to a light continental indenter (analog for the Indian continent). The subduction fault (plates interface) is lubricated with lubricant paste (petroleum jelly), and glucose syrup is filling a small space comparable to a weak zone (Figure 2). The distance between the plates filled by glucose syrup is variable during the first 4–5 min of the experiment but rapidly stabilizes at approximately 2 mm. The use of a weak subduction fault is required in order to have a continuous one-sided subduction [*Faccenda et al*., 2008; *De Franco et al*., 2008; *Sokoutis and Willingshofer*, 2011]. This configuration is similar to the low-coupling models of *Iaffaldano et al*. [2012]. In some experiments, the initial configuration is completed by lateral oceans, analog for Makran and Indonesian domains on each side (Figure 1). Silicone putties are viscoelastic materials, quasi-

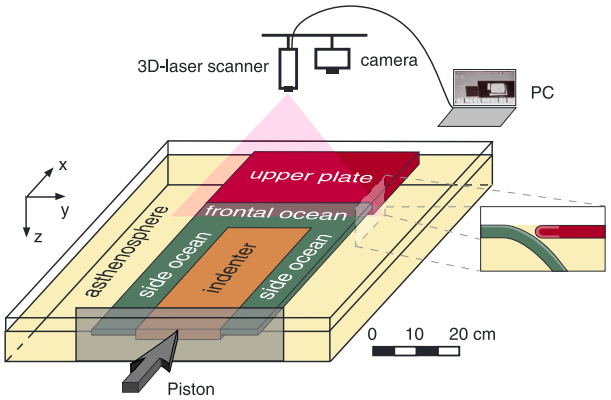

Figure 2. Experimental setup. Some experiments were performed only with the frontal ocean, others with both frontal and side oceans (Table 3). The subduction fault (plates interface) is lubricated with lubricant paste (petroleum jelly, in light colors), and glucose syrup is filling a small space between the plates, comparable to a weak zone.

Newtonian at experimental strain rates [*Weijermars*, 1986] and the glucose syrup a Newtonian fluid. The properties of analog materials are listed in Table 1. The subducting plate is attached to a rigid piston advancing at constant velocity and reproducing the convergence between India and Asia. The piston is confined to the upper part of the tank, and the glucose syrup is free to move underneath.

[6] The model is placed in a Plexiglas box ($75 \times 75 \times 25$ cm^3) with the overriding plate attached to the fixed back wall, far enough from the box sides to minimize boundary effects [*Funiciello et al.*, 2006]. The experiments are properly scaled for gravity, length, density, viscosity, and velocity following the method of previous studies [e.g., *Weijermars and Schmeling*, 1986; *Davy and Cobbold*, 1991; *Funiciello et al.*, 2003]. The scaling factor for length is 1.7×10^{-7} so that 1 cm of the model corresponds to 60 km in nature. The density and viscosity ratios between the oceanic silicone putty and asthenospheric glucose syrup are 1.05 and 1.5×10^3, respectively. The piston's velocity of 0.54 cm min^{-1} is scaled to correspond to 5.7 cm yr^{-1} of convergence in nature, and 1 min in experimental time corresponds to 0.55 My in nature. Further details on scaling procedures are presented in Table 2.

[7] Our models are performed with the following assumptions and consequent limitations as described in *Funiciello et al.* [2003]: (1) isothermal system (we neglect thermal diffusion and phase changes), (2) the viscosity and density are constant with depth in each individual layer, (3) lack of global background mantle flow, (4) the bottom of the Plexiglas tank simulates the 660 km discontinuity considered as an impermeable barrier, (5) the models do not include any brittle upper layer, the lithospheres being modeled only by silicone putties. This material is scaled to the bulk viscosity of the lithosphere in nature as well as density and viscosity ratios between lithosphere and asthenosphere (Table 2) and reproduces a linear viscous behavior. Thus, although no localization of the deformation occurs, this setup allows us to reproduce subduction dynamics and overall strain patterns comparable to natural systems.

[8] Each experiment is monitored over its entire duration by top- and lateral-view photos taken at regular time intervals. Topography evolution is recorded by a laser scanner (Real Scan USB) whose precision is 0.1 mm corresponding to 600 m in nature. A squared grid of passive markers drawn on the silicone layers enables visualization of the surface deformation.

[9] For representative experiments, we compute the displacement field for a small increment of deformation (over a 1 min time step). We used the procedure Cosi-Corr integrated to the software ENVI, made for subpixel correlation of images [*Leprince et al.*, 2007; *Ayoub et al.*, 2009]. This procedure correlates 1 pixel of the picture of step n with 1 pixel of the picture of step $n+1$ using a window moving across the picture. The result is the displacement field between both steps. We used Cosi-Corr frequency parameters depending on the experiments of 128 or 64 pixels for initial window size (size of initial search zone around the considered pixel), 32 or 16 pixels for final window size, and 16 pixels for step (one measurement each 16 pixels of the picture).

2.2. Forces Equilibrium

[10] In collisional systems, the growth and shape of the mountain belt is controlled by the equilibrium between body and boundary forces [*England and McKenzie*, 1982]. Boundary forces are the driving forces favoring collision, whereas buoyancy forces resist it.

2.2.1. Driving Forces

[11] The two main driving forces are the tectonic force (F_t) and the slab pull (F_{sp}). The tectonic force applied at the plate boundary produces the motion of the indenting plate toward the collision zone. In nature, the motion of the indenter could be also supported by far-field stress related to plume push [*van Hinsbergen et al.*, 2005], ridge push [*Ghosh et al.*, 2010], or mantle drag generated by a large-scale convection cell [*Alvarez*, 2010; *Becker and Faccenna*, 2011]. In our experiments, we simulate the far-field stress with a piston pushing the indenter at constant rate. The slab-pull force depends on the slab buoyancy given by the density contrast between lithosphere and asthenosphere, and the slab volume (i.e., length and width). The oceanic slab is denser than the asthenosphere, and when its length increases as oceanic subduction goes on, F_{sp} becomes more negative (increasing negative buoyancy) favoring extensional backarc basin formation [e.g., *Funiciello et al.*, 2003]. When the lighter continental slab enters the trench and subducts, F_{sp} increases toward positive values (increasing positive buoyancy). Our model setup using a mean viscosity for the continental lithosphere leads to a continuous continental subduction, equivalent to the subduction observed after the scraping off of the upper crust by *Capitanio et al.* [2011], showing that the force balance is similar. During continental subduction, the trench switches

Table 1. Properties of Experimental Materials

Material	Density (kg m^{-3})	Viscosity[a] (Pa s)
Black ocean	1495	3.4×10^4
Indenter (silicone 4)	1411	4.9×10^4
Light indenter (silicone 6)	1388	
Black continent	1364	3.2×10^4
Weak black continent	1350	3×10^4
White continent	967	1×10^4
Intermediate syrup (asthenosphere)	1428	22

[a]Viscosities are given for room temperature (22°C) and an experimental strain rate of 10^{-2} s^{-1} (scaled for nature).

Table 2. Scaling of Parameters for the Reference Experiment (SH7)

	Parameter	Nature	Model
g	Gravitational acceleration ($m\,s^{-2}$)	9.81	9.81
Thickness[a]			
h_c	Continental lithosphere (m)	100,000	0.016
h_o	Oceanic lithosphere (m)	70,000	0.012
h_{asth}	Upper mantle asthenosphere (m)	660,000	0.11
Density			
ρ_c	Continental lithosphere ($kg\,m^3$)	3,200	1,411
ρ_o	Oceanic lithosphere ($kg\,m^3$)	3,320	1,495
ρ_{asth}	Upper mantle asthenosphere ($kg\,m^3$)	3,220	1,428
ρ_c/ρ_{asth}	Density ratio continent	0.99	0.99
ρ_o/ρ_{asth}	Density ratio ocean	1.04	1.05
Viscosity			
η_c	Continental lithosphere (Pa s)	10^{23}	4.9×10^{4}
η_o	Oceanic lithosphere (Pa s)	10^{24}	3.4×10^{4}
η_{asth}	Upper mantle asthenosphere (Pa s)	10^{21}	22
η_c/η_{asth}	Viscosity ratio continent	10^{2}	2.2×10^{3}
η_o/η_{asth}	Viscosity ratio ocean	10^{3}	1.5×10^{3}
	Dimensionless parameters		*Equivalence model-nature*
$t°$	Characteristic time: $(t_{model}/t_{nature}) = (\Delta\rho gh)_{lith\ nature}/(\Delta\rho gh)_{lith\ model} \times (\eta_{l\ model}/\eta_{l\ nature})$		3.46×10^{-12} $1\ min_{model} \rightarrow 0.55\ My_{nature}$ $1\ h_{model} \rightarrow 33\ My_{nature}$
$U°$	Characteristic velocity: $(U_{model}/U_{nature}) = t_{nature}/t_{model} \times L_{model}/L_{nature}$		49,563 $1\ cm\,h^{-1}{}_{model} \rightarrow 0.18\ cm\,y^{-1}{}_{nature}$

[a]Scale factor for length $L_{model}/L_{nature} = 1.7\times10^{-7}$.

to either stationary or advancing regime [*Bellahsen et al*., 2003; *Regard et al*., 2003; *Magni et al*., 2012]. In this case, positive slab-pull force may favor continental collision, even though the amount of trench advance is always rather limited [*Magni et al*., 2012]. Events such as break-off of the dense oceanic root attached to the continental slab favors trench advance and collision since slab pull is no longer effective to drive trench retreat [*Chemenda et al*., 2000; *Wortel and Spakman*, 2000; *Regard et al*., 2003; *Replumaz et al*., 2010b]. However, such mechanism is not reproducible with our model setup and will not be considered in this paper.

2.2.2. Resisting Forces

[12] Resisting forces in the system are the forces acting at the plates interface. We can distinguish the coupling (R_f), the bending resistance of the plate (R_b), the resistance to sliding in the mantle (R_s), and the buoyancy of the upper plate (F_b). They depend on the nature of the plates and trench motion, as previously quantified in experimental studies [e.g., *Becker et al*., 1999; *Bellahsen et al*., 2005; *Funiciello et al*., 2008]. In our viscous simplified system, R_f is proportional to the plate thickness and the viscosity of the plate interface, considered of the same order as the asthenospheric mantle. The geometry of the subduction interface is shown in Figure 2, and viscosities of the asthenospheric mantle (η_s) depending on temperature (T_s) for each experiment are reported in Table 3. These parameters will influence the lubrication of the subduction zone and can lead to an efficient or inefficient subduction. Computations of the frictional shear stress range between 15 and 30 MPa and contribute for ~10–30% of the energy dissipated during subduction [*Zhong and Gurnis*, 1994]. The viscous dissipation at the trench scales with the plate's strength (i.e., viscosity) and thickness and is inversely proportional to the cube of the radius of curvature [*Conrad and Hager*, 1999; *Becker et al*., 1999]. It may contribute for about 10 to 30% of the energy dissipated during subduction. The resistance to bending R_b is proportional to the viscosity, the cube of the thickness of the slab and the velocity of subduction, and inversely proportional to the cube of the radius of curvature of the subducting plate [*Turcotte and Schubert*, 1982; *Becker et al*., 1999]. The resistance to subduct *Rs* represents the viscous dissipation exerted at the slab-mantle interface during subduction and is directly proportional to the area of the slab surface and asthenosphere viscosity.

[13] The last resisting force is produced by the buoyancy of the continental plate. During continuous thickening, the upper plate stores potential energy with respect to the lowlands (i.e., subducting plate) generating a differential stress. Following *Artyushkov* [1973], *Turcotte* [1982], and *Stein et al*. [1989], the force per unit length due to potential energy scales with the gravity and the density contrast of the upper plate with respect to the mantle and its thickness. This stress generates the deformation of the upper plate, which in our case is distributed. Only ductile strain is monitored as no brittle layers have been used. This strain is proportional to upper plate viscosity.

2.2.3. Buoyancy Number

[14] The dimensionless ratio between the buoyancy of the upper plate ($\Delta\rho gH$) and its resistance to deformation ($\eta d\varepsilon/dt$) can be expressed as a buoyancy number (F_b), similar to the Argand number [*England and McKenzie*, 1982]. This number is expected to vary with time during progressive thickening or thinning of the plate and can be written as

$$F_b = \Delta\rho g H_i f/(\eta d\varepsilon/dt) \quad (1)$$

where $\Delta\rho$ is the density contrast between the upper plate and the asthenosphere, g the gravity acceleration, H_i and η the initial thickness and viscosity of the plate, respectively, $d\varepsilon/dt$ the experimental strain rate, and f the thickening factor

Table 3. Experimental Parameters for Each Experiment

Experiment set	Continental Plates (Upper Plate Silicone, Size in cm)[a]	Size of Frontal Oceanic Plate (cm)	Size of Side Oceanic Plates (cm)	Thickness (cm)[a]	Curvature at 40 min (cm)[b]	Trench Temperature (°C)	Trench Viscosity (Pa s)	Buoyancy Number
SH6	UP (BC): 40 × 20 Ind: 20 × 25	40 × 4	10 × 25	UP: 0.6 Ind: 1.20 ocean: 1.2	4.3	21	46	0.8
SH7	UP (BC): 40 × 20 Ind: 20 × 25	40 × 7	None	UP: 0.55 Ind: 1.13 ocean: 1.26	1	21.6	42.5	0.7
SH8	UP (BC): 55 × 20 Ind: 35 × 25	35 × 7	None	UP: 0.8 Ind: 1.10 ocean: 1.3	−1.1	23.1	34.5	1.4
SH9	UP (WBC): 40 × 20 Ind: 20 × 25	20 × 7	None	UP: 0.75 Ind: 1.16 ocean: 1.18	−0.2	23.1	34.5	1.7
SH10	UP (WBC): 40 × 20 Ind: 20 × 25	20 × 7	None	UP: 0.58 Ind: 1.2 ocean: 1.18	−0.5	21.9	41.5	1.0
SH11	UP (WBC): 40 × 20 Ind: 20 × 25	20 × 7	None	UP: 0.57 Ind: 1.18 ocean: 1.12	0.8	23.1	35	1
SH12	UP (WBC): 40 × 20 Ind: 20 × 25	20 × 10	None	UP: 0.6 Ind: 1.18 ocean: 1.05	1.6	24	30	1.1
SH13	UP (WC): 40 × 20 Ind: 20 × 25	20 × 7	None	UP: 1.9 Ind: 1.47 ocean: 1.16	−1.3	26.3	18.5	181.4
SH14	UP (WC): 40 × 20 Ind: 20 × 37	20 × 7	None	UP: 0.6 Ind: 1.22 ocean: 1.19	1	22.3	39	18.1
SH15	UP (WC): 40 × 20 Ind: 20 × 37	20 × 7	None	UP: 0.64 Ind: 1.2 ocean: 1.17	1.7	21.8	42	20.8
SH16	No UP Ind: 20 × 37	20 × 7	None	Ind: 1. ocean: 1.07		21.2	44.5	
SH17	UP (WC): 40 × 20 Ind: 20 × 37	20 × 7	None	UP: 1.88 Ind: 1.17 ocean: 1.21	0.9	21.5	43.5	177.6
SH18	UP (WC): 40 × 20 Ind: 20 × 37	20 × 5	None	UP: 1.98 Ind: 1.27 ocean: 1.18	−0.4	21.7	42	197
SH19	UP (WC): 40 × 20 Ind (light): 20 × 37	20 × 7	None	UP: 1.9 Ind: 1.28 ocean: 1.28	−0.5	21.3	44.5	181.4
SH20	UP (WC): 40 × 20 Ind: 20 × 37	20 × 7	10 × 37	UP: 1.93 Ind: 1.22 ocean: 1.15	−1.3	24.2	30	187.2
SH21	UP (WC): 40 × 20 Ind: 20 × 37	20 × 7	10 × 37 + lateral cuts [c]	UP: 1.90 Ind: 1.27 ocean: 1.26	1	19.8	53	181.4
SH22	UP (BC): 40 × 20 Ind: 20 × 37	20 × 7	None	UP: 0.60 Ind: 1.20 ocean: 1.14	−1.9	24.1	29.5	0.8

Table 3. (continued)

Experiment set	Continental Plates (Upper Plate Silicone, Size in cm)[a]	Size of Frontal Oceanic Plate (cm)	Size of Side Oceanic Plates (cm)	Thickness (cm)[a]	Curvature at 40 min (cm)[b]	Trench Temperature (°C)	Trench Viscosity (Pa s)	Buoyancy Number
SH23	UP (sil. 4): 40 × 20 Ind: 20 × 37	20 × 7	None	UP: 0.56 Ind: 1.20 ocean: 1.16	−1.6	24.2	29	0.1

[a]UP: upper plate; Ind: indenter; BC: Black continent; WBC: weak black continent; WC: white continent.
[b]Curvature is measured as shown in Figure 1. The value is positive when it is concave (toward the north) and negative when it is convex (toward the south).
[c]In experiment SH21, we cut between lateral oceans and indenter to allow free motion along this limit.

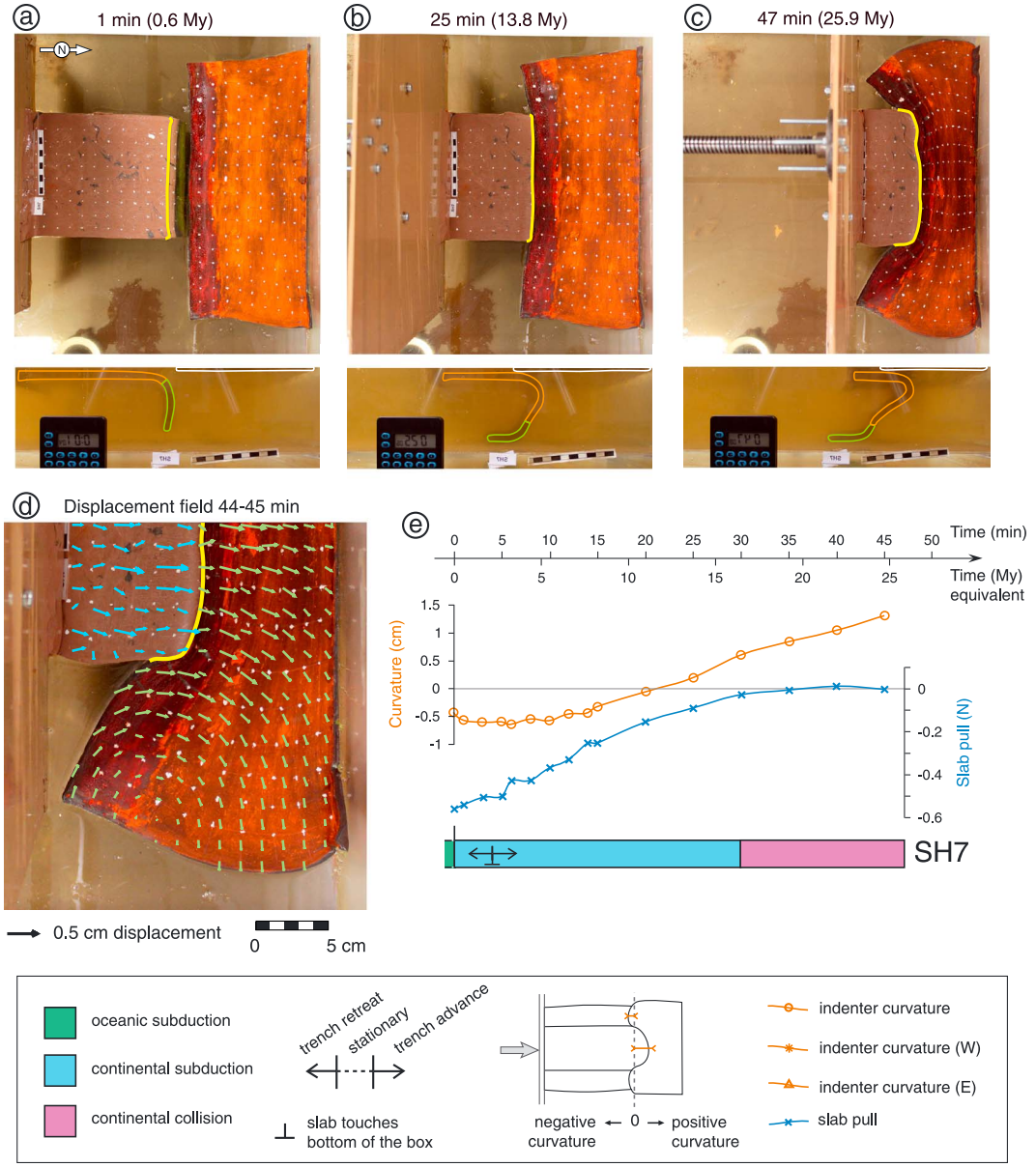

Figure 3. (a, b, and c) Top- and side-view photos of experiment SH7 at 1 min, 25 min, and 47 min, respectively. On top views, the solid yellow line highlights trench location and shape. On side views, oceanic slab is outlined in green, continental slab in orange, upper plate in white. (d) Displacement field computed with Cosi-Corr plugin (see text for details) over a 1 min time-step. (e) Timeline illustrating the main phases of subduction and collision, with evolution of curvature and slab pull over time. The amplitude of curvature is measured as shown on the sketch in the legend. Curvature is positive when concave, negative when convex.

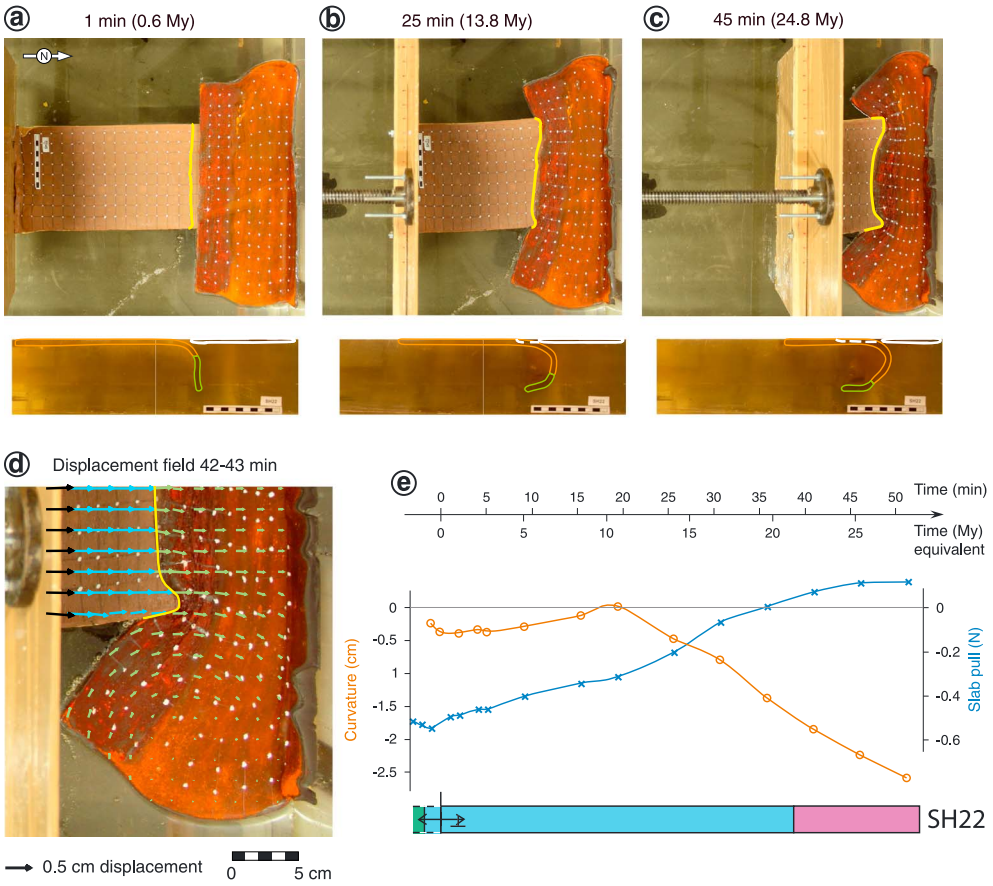

Figure 4. (a, b, and c) Top- and side-view photos of experiment SH22 at 1 min, 25 min, and 45 min, respectively. (d) Displacement field. (e) Timeline, curvature, and slab-pull evolution. Legend is the same as for Figure 3.

measured in the center of the upper plate. The strain rate is calculated as

$$d\varepsilon/dt = v/H_i \tag{2}$$

where v is the piston velocity. The thickening factor allows us to estimate the evolution of the buoyancy number through time and is calculated as

$$f = H_f/H_i \tag{3}$$

where H_f is the thickness at the considered stage. The method used for thickness calculation is detailed in Appendix A. From equations (2) and (3), (1) is equivalent to

$$F_b = \Delta\rho g H_i H_f/\eta v \tag{4}$$

3. Experimental Results: Generating Curvature and Syntaxes

[15] We performed 21 experiments varying geometrical and rheological parameters and selected 16 whose characteristics are listed in Table 3. By analogy with India-Asia collision, we shall refer thereafter to regions of the experiment in terms of geographical directions, the southern boundary corresponding to the piston that is moving toward the north (i.e., from left to right in all figures).

[16] For each experiment, we observed three successive processes, the subduction of the frontal ocean, the subduction of the light continental indenter pulled by the denser oceanic slab, and finally the continental collision when the continental lithosphere stops sinking vertically into the mantle. We classified the experiments in different sets. The first set includes experiments with a buoyancy number of 0.5 to 3 where the thickening of the upper plate is large, the second set experiments with a buoyancy number of 20 to 170 where the lateral escape of the upper plate is large, and the third set includes experiments with lateral oceans on each side of the indenter simulating Makran and Indonesian subduction zones. In each set, we tested the influence of the viscosity of the upper plate and efficiency of the subduction.

[17] We first present three experiments from the first set. SH7 is our reference experiment (Table 3).

3.1. First Set (Low F_b), Inefficient Subduction (SH7)

[18] The reference experiment SH7 is composed of an upper plate ("black continent" silicone appearing as red) of $40 \times 20 \times 0.55$ cm^3 and a subducting plate made of an oceanic plate ("black continent" silicone appearing in green, $40 \times 7 \times 1.26$ cm^3) attached to a continental indenter (pink silicone) of $20 \times 25 \times 1.13$ cm^3 (Figure 1). The buoyancy number at the onset of the experiment is 0.7 (Table 3). The viscosity of the trench is 42.5 Pa s corresponding to a poorly lubricated trench.

[19] The experiment starts by the subduction of the oceanic silicone located at the front of the subducting plate accompanied

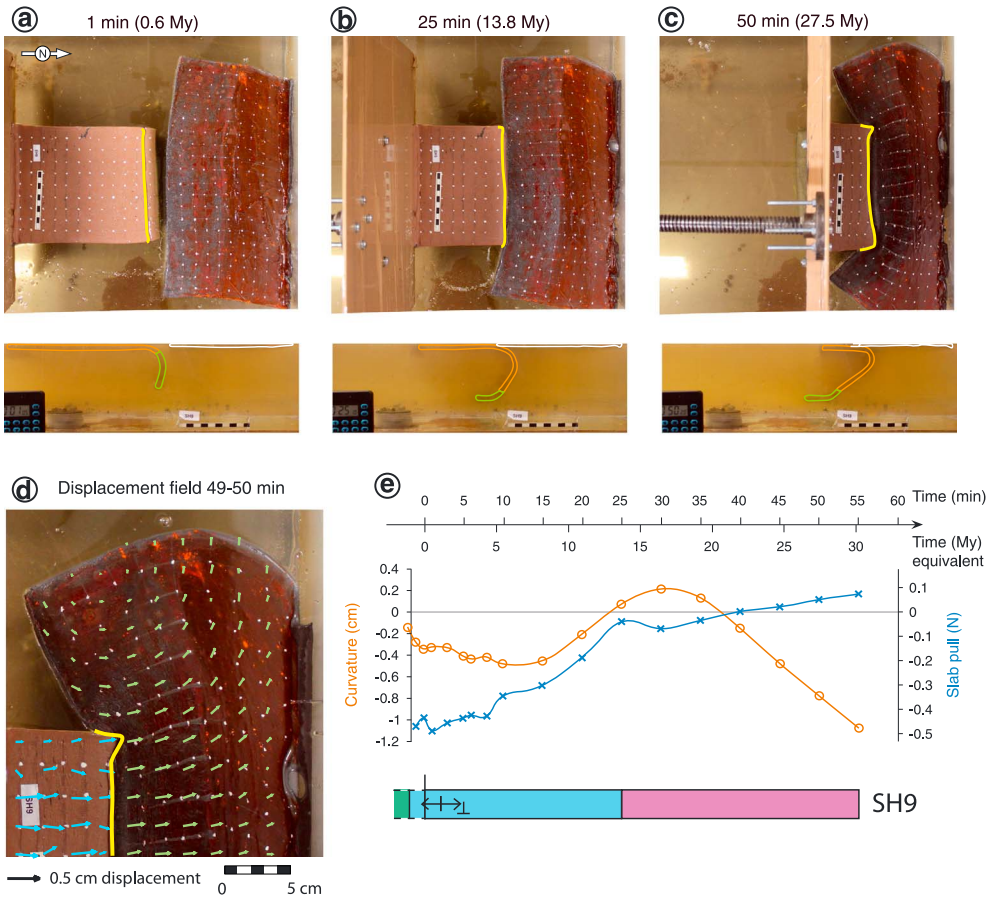

Figure 5. (a, b, and c) Top- and side-view photos of experiment SH9 at 1 min, 25 min, and 50 min, respectively. (d) Displacement field. (e) Timeline, curvature, and slab-pull evolution. Legend is the same as for Figure 3.

by trench retreat (Figure 3). Subduction is driven by the negative buoyancy of the slab and the push of the advancing piston. The trench gently curves toward the south (Figures 3a and 3e) due to active toroidal flow around the corners of the downgoing plate producing along-strike variations in subduction velocity [*Funiciello et al.*, 2006]. Importantly, it generates a small perturbation at each extremity of the downgoing plate, similar to a proto-syntaxis. At the beginning of continental subduction, buoyant material enters the trench and changes the force equilibrium: slab pull decreases in magnitude (Figure 3e) and the trench advances. The curvature remains oriented toward the subducting plate during early continental subduction (Figure 3e). When slab pull approaches zero, subduction becomes less efficient and the trench adopts a straight shape (Figure 3b), which progressively reverses to form a concave arc without syntaxes (Figure 3c). Finally, when the buoyancy of the slab becomes positive, the trench locks, no more material subducts, and continental collision initiates. The curvature amplifies during the continental collision phase. It generates an indentation opposite to the Himalayan curvature without any syntaxis.

[20] The displacement field in the upper plate is dominated by N-S shortening in the center of the model that rotates NW-SE and NE-SW in the northwestern and northeastern corners, respectively (Figure 3d). We measure the partitioning of the convergence along a midnorth-south line after 40 min of piston advance (Appendix B). We conclude that in the north-south direction, the convergence is accommodated at 52% by continental subduction, 38% by shortening of the upper plate and 10% by shortening of the indenter.

3.2. First Set (Low F_b), Efficient Subduction (SH22)

[21] Experiment SH22 has a buoyancy number similar to SH7 ($F_b = 0.8$) but differs by a higher temperature of the glucose syrup. The viscosity of the syrup is thus lower, which generates a more efficient lubrication of the trench and efficient subduction. The early evolution is the same as SH7: the trench forms a convex arc during oceanic subduction, with a proto-syntaxis at each extremity (Figures 4a and 4e). As for SH7, the early convex curvature decreases slowly during continental subduction and reaches an almost straight shape, while the proto-syntaxes perpetuate, although smaller in amplitude (Figure 4e). The trench did not lock at the onset of collision as in experiment SH7, and the continental subduction is continuous. The slab pull increases continuously, and when it approaches a positive value at approximately 20 min (11 My), the trend reverses and both the curvature and proto-syntaxes amplify, forming an orocline convex toward the south (Figures 4b and 4e). Although the slab does not sink vertically anymore, a little amount of continent is forced to subduct, forming a rather flat slab in late stages (underthrusting). The more efficient lubrication of the trench allows more continent to subduct despite the positive buoyancy of the slab,

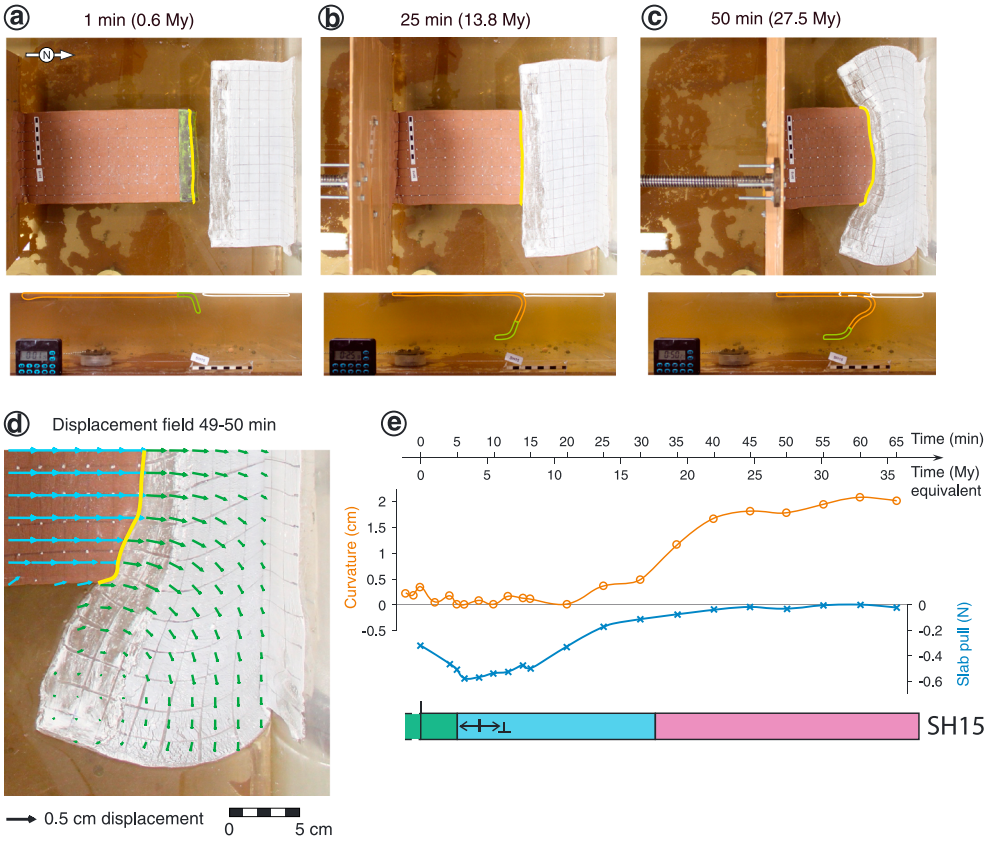

Figure 6. (a, b, and c) Top- and side-view photos of experiment SH15 at 1 min, 25 min, and 50 min, respectively. (d) Displacement field. (e) Timeline, curvature, and slab-pull evolution. Legend is the same as for Figure 3.

driven by the push of the piston combined with the anchor of the oceanic slab. As for SH7, the displacement field in the upper plate is dominated by N-S shortening in front of the indenter that rotates on each side (Figure 4d). The difference in N-S shortening between the center of the indenter and its sides results in a relative transversal flow of upper plate material overthrusting the subducting plate. This transversal flow enhances the convex orocline and the development of syntaxes during collision (Figures 4c and 4e).

[22] After 40 min of experiment (equivalent to 22 My), the convergence has been accommodated in the N-S direction by subduction (41%), shortening of the upper plate (36%), and of the indenter (23%).

3.3. First Set (Low F_b), Efficient Subduction, Weak Upper Plate (SH9)

[23] Experiment SH9 is similar to SH22 but performed with a weaker upper plate to test the influence of its viscosity (Table 3). The early stages of oceanic and continental subduction are similar to that of experiment SH22 with the formation of proto-syntaxes and a convex arcuate trench (Figure 5a), which progressively straightens during late continental subduction (Figures 5b and 5e). However, unlike SH22, it passes through a concave stage correlating with an almost zero slab-pull force (neutral buoyancy; Figure 5e). Similarly to SH22, when the slab pull reaches positive values, the curvature evolution reverses to a convex shape that is amplified during continental collision (Figures 5c and 5e). The upper plate undergoes N-S shortening at the orogenic front, E-W extension in the central area of the plate, and rotation at the free edges as shown on the velocity field (Figure 5d), similar to that of SH22. After 40 min of experiment (22 My), 54% of the convergence has been accommodated at the trench, 26% by N-S shortening of the upper plate, 20% by that of the indenter.

3.4. Second Set (High F_b), Inefficient Subduction, Weak Upper Plate (SH15)

[24] In experiment SH15, we used an upper plate 3 times weaker than for SH7 to further explore the influence of rheology. This experiment has a high buoyancy number ($F_b = 20.8$). The main effect of the weaker silicone is to favor gravitational collapse (Figure 6). The viscosity of the trench is 42 Pa s leading to poor lubrication and inefficient subduction.

[25] The subduction stage is rather different from SH7, with a constant straight shape of the trench in early stages. When the slab pull approaches zero (neutral buoyancy of the slab), the trench curves concavely. During collision, the orocline grows and produces a moderate indentation (Figure 6). Despite a viscosity of the upper plate lower than for SH9, the poor lubrication of the trench prevents efficient overthrusting. The final curvature is concave and no syntaxes are formed, as for experiment SH7. The orogenic front is characterized by N-S shortening, while lateral escape and rotation predominate at the edges of the upper plate (Figure 6d). The total thickening is lower than for the first set of experiments and compensated by a larger amount of lateral escape. The subduction undertakes

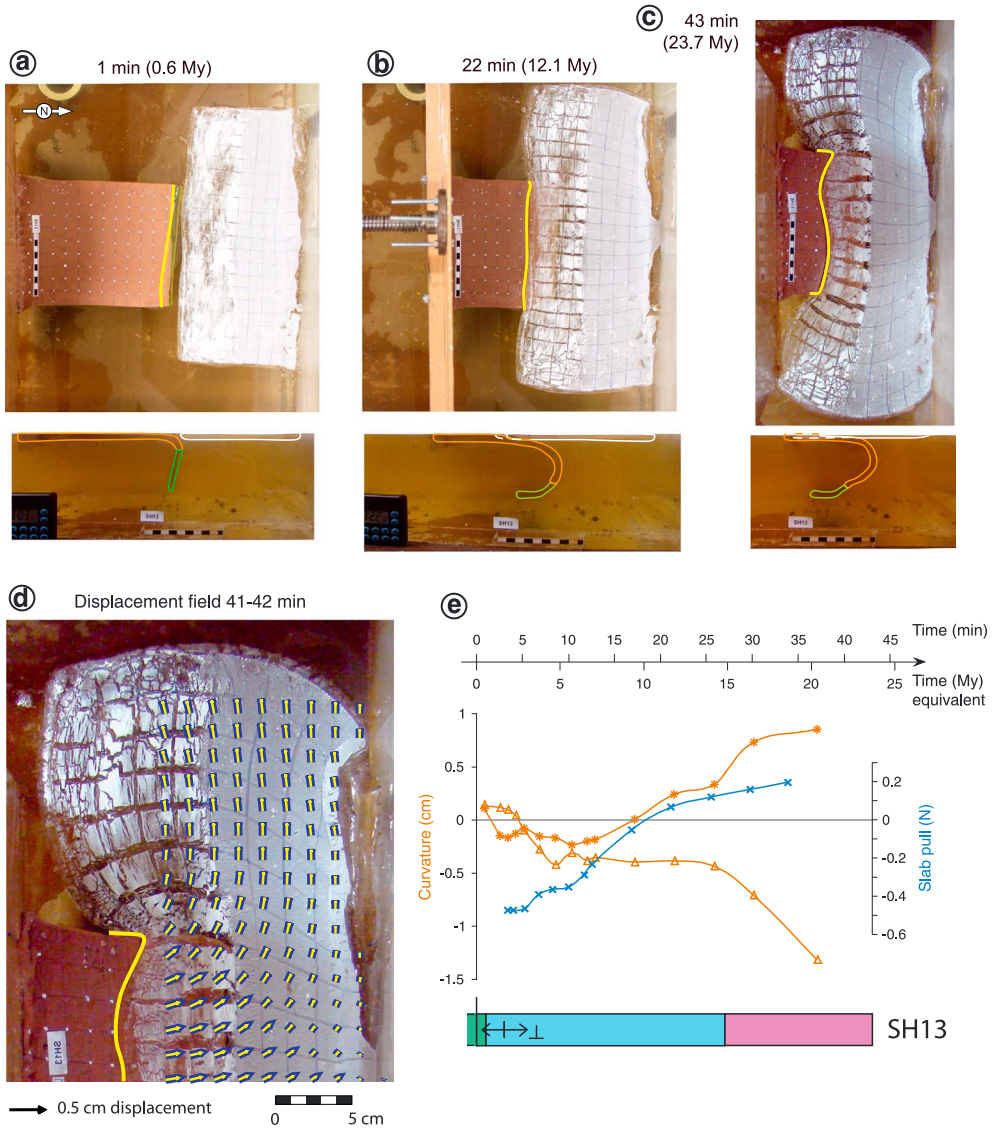

Figure 7. (a, b, and c) Top- and side-view photos of experiment SH13 at 1 min, 22 min, and 43 min, respectively. (d) Displacement field. (e) Timeline, curvature, and slab-pull evolution. Legend is the same as for Figure 3.

62% of the convergence, N-S shortening of the upper plate 28%, and N-S shortening of the indenter 10%.

3.5. Second Set (High F_b), Efficient Subduction, Thick and Weak Upper Plate (SH13)

[26] Experiment SH13 has one of the highest buoyancy numbers ($F_b = 181.4$), due to thicker upper plate compared to SH15 (Table 3). The viscosity of the trench is 18.5 Pa s leading to good lubrication of the plates interface.

[27] As in reference experiment SH7, the trench forms a convex arc during oceanic subduction and early continental subduction (Figures 7a and 7e). Due to an experimental bias (the silicones of the subducting and upper plate stick together in one point on the eastern part of the trench), the evolution then becomes asymmetric. Only one syntaxis forms on the western corner of the downgoing plate, where the subduction is continuous. The eastern half of the trench curves concavely where the trench locks. For both sides, the major change in curvature orientation occurs when, or soon after, the buoyancy reaches positive values (Figures 7c and 7e). In the region of convex orocline, the curvature rapidly accentuates during continental collision as overthrusting is amplified by a collapse of the overriding plate over the subducting plate (as observed in the first set). This overthrusting and the final convex curvature are more pronounced than in previous experiments due to the higher buoyancy number (i.e., higher gravitational potential energy).

[28] The collapse dynamics of the system is confirmed by the displacement field that indicates global E-W extension on a large area of the upper plate (Figure 7d). As a consequence, most of the convergence is accommodated by subduction (83%), only 10% by N-S shortening of the upper plate, and 7% by that of the indenter.

3.6. Third Set (Lateral Oceans), Low F_b, Inefficient Subduction (SH6)

[29] In the third set, we add lateral oceans to the indenter (Figure 2). We will present two end-member cases: one with a low buoyancy number and poorly lubricated trench (SH6;

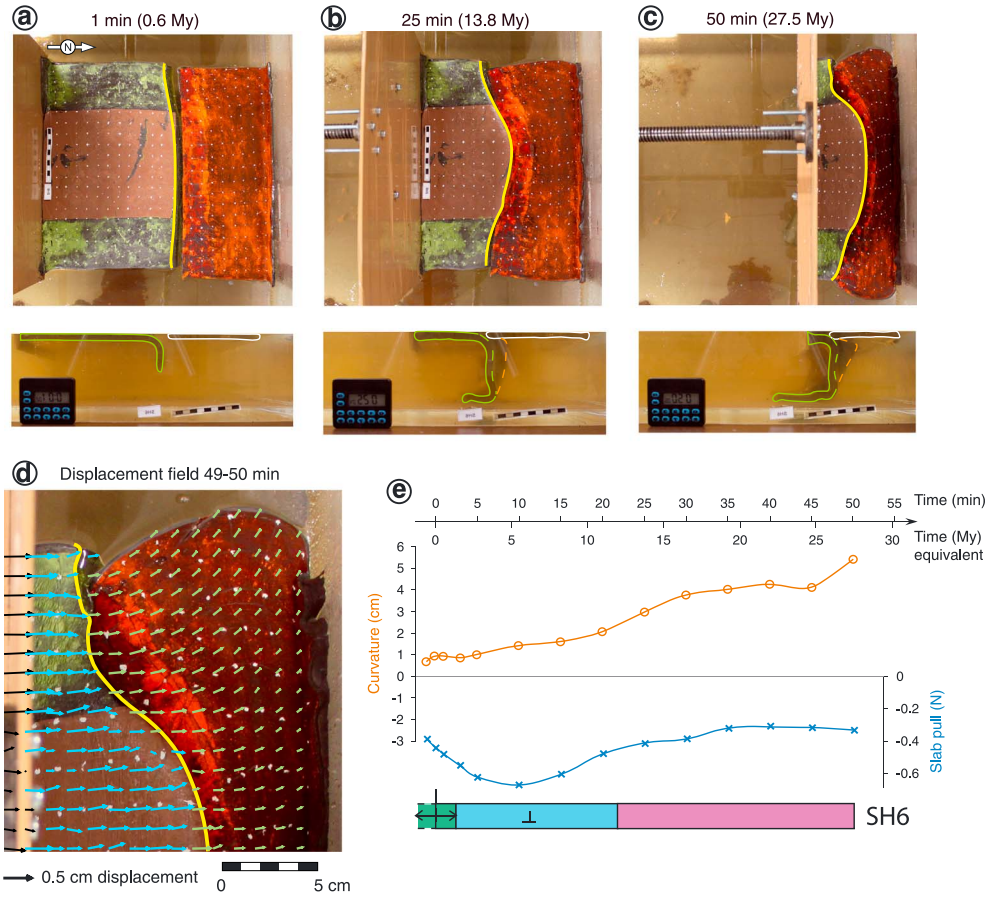

Figure 8. (a, b, and c) Top- and side-view photos of experiment SH6 at 1 min, 25 min, and 50 min, respectively. (d) Displacement field. (e) Timeline, curvature, and slab-pull evolution. Legend is the same as for Figure 3.

Figure 8) and the other with a high buoyancy number and well-lubricated trench (SH20; Figure 9).

[30] In experiment SH6, the upper plate is made of black silicone identical to that of SH7 (Table 3). The buoyancy number is low ($F_b = 0.78$) and the viscosity of the subduction interface is high (46 Pa s) leading to poor lubrication.

[31] The experiment starts by the subduction of the oceanic silicone located at the front of the subducting plate accompanied by trench retreat. The trench acquires a slightly concave shape during this phase as trench retreat is faster on the sides (Figure 8a). This curvature is then accentuated during the continental subduction stage. Oceanic subduction proceeds on the sides while lighter indenter (continent) is subducted at the center. Entrance of buoyant material at the trench changes the force equilibrium: slab pull continues to increase on the sides that still undergo trench retreat but decreases at the center that switches to trench advance. The difference in slab-pull force and hence trench motion leads to a more pronounced concave curvature (Figure 8b). The orocline shape is finally amplified during the entire continental collision phase (Figures 8c and 8e) and generates a large indentation (approximately 40% of the final length) opposite to the Himalayan curvature; no syntaxes are formed.

[32] The displacement field in the upper plate is dominated by N-S shortening in the center of the model that rotates NW-SE and NE-SW in the northwestern and northeastern corners, respectively (Figure 8d). However, the rotational component is less important than in experiments without side oceans. After 40 min of experiment (22 My), the convergence has been undertaken at 62% by the subduction and 38% by shortening of the upper plate.

3.7. Third Set (Lateral Oceans), High F_b, Efficient Subduction (SH20)

[33] Experiment SH20 is performed with a weak upper plate (white continent) as thick as SH13 and three times thicker than SH15 (Table 3). This experiment has the highest buoyancy number ($F_b = 187$), almost 10 times that of SH15, similar to SH13. The viscosity of the trench is 44.5 Pa s, leading to poor lubrication.

[34] The stages of oceanic subduction and early continental subduction are comparable to SH6 with a difference in trench velocity between the center (light continent) and the sides (dense oceanic lithosphere) leading to a concave orocline (Figures 9a and 9e). However, the curvature of the indenter reverses rapidly and becomes convex toward the south as the overriding plate overthrusts the center of the continent. Between lateral oceans subducting vertically and the overflowed center of the continent, the edges of the continent form proto-syntaxes (Figure 9c). This change is amplified during continental collision as slab pull approaches zero. At the end of the experiment, we observe two syntaxes wider than in experiments without side oceans (Figures 9c and 9e). The upper plate also undergoes pronounced lateral flow (Table 3).

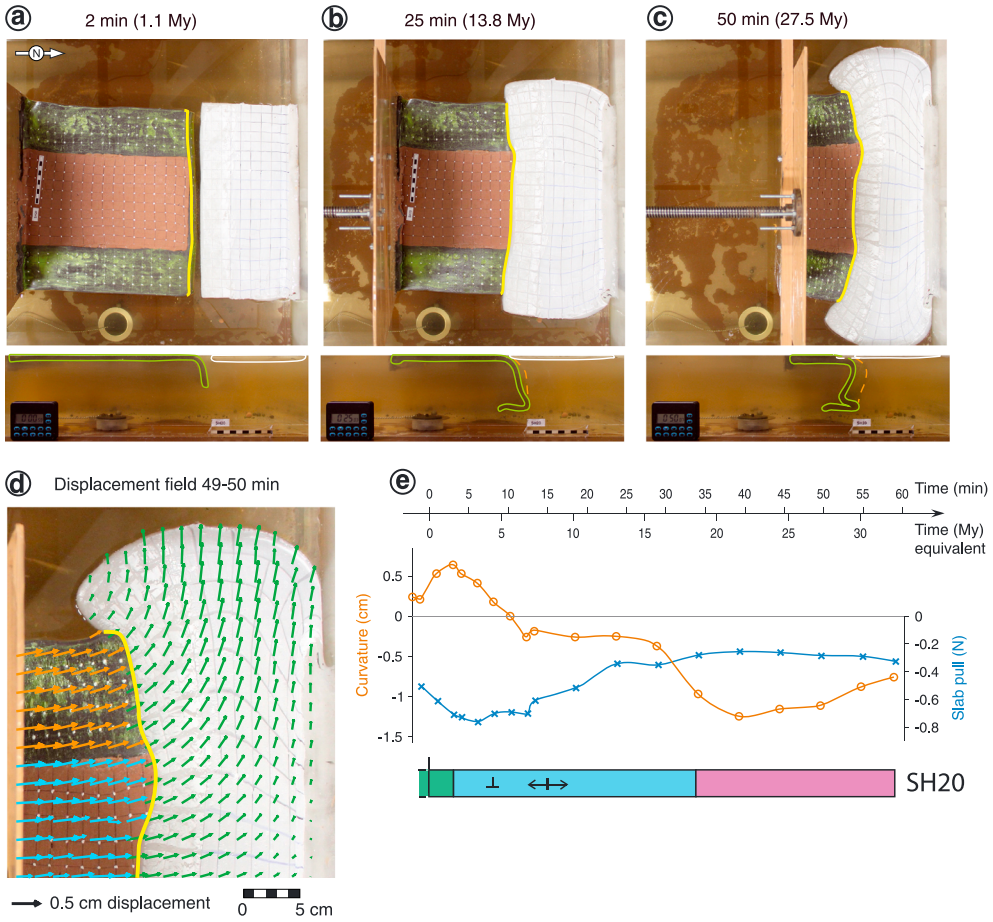

Figure 9. (a, b, and c) Top- and side-view photos of experiment SH20 at 2 min, 25 min, and 50 min, respectively. (d) Displacement field. (e) Timeline, curvature, and slab-pull evolution. Legend is the same as for Figure 3.

[35] Deformation of the upper plate is dominated by N-S shortening and E-W lateral escape. We also observe a very limited rotation of the extremities of the upper plate (Figure 9d).

4. Discussion: Range Shape Evolution

[36] The continental lithosphere has long been considered too buoyant to subduct on its own, and even when attached to a dense oceanic slab, break-off should occur once the continent enters the trench [*Ton and Wortel*, 1997; *Chemenda et al.*, 2000; *Regard et al.*, 2003]. However, by correlating the positive wavespeed tomographic anomalies with the position of the suture through time, it has been shown that pieces of the Indian continent have subducted in the mantle [*Replumaz et al.*, 2010a]. Our models successfully reproduce continuous continental subduction with a light indenter attached to a dense oceanic plate as shown in numerical models with a continent scraped off its upper crust and part of its lower crust [*Capitanio et al.*, 2011]. Proto-syntaxes at each extremity of the subducting plate and slight convex curvature initiate during continental subduction that either grows or is repressed during collision. This evolution and the final amplitude of the curvature appear to be controlled by three main parameters: the efficiency of the subduction (that is apparently correlated to the viscosity of the plates interface), the buoyancy number of the upper plate, and the lateral decoupling.

4.1. Subduction Efficiency

[37] During our experiments, we observed that similar experiments give opposite curvature of the trench for low or high temperature of the glucose syrup located at the trench. The room temperature causes negligible variation of silicone viscosity (maximum 10% of variation for a decrease of 5°C) but not negligible for glucose syrup (130% of variation for a 5°C decrease). A similar decrease has been recently measured for the lubricant paste used at the trench [*Duarte et al.*, 2013]. It appears empirically to be a determinant parameter for the trench curvature. We interpret the viscosity of the asthenosphere to correspond to the viscosity of the subduction interface and influencing the lubrication efficiency of the subduction zone. If the viscosity of the trench is high (> 35 Pa s), the subduction interface is poorly lubricated. The continental subduction will tend to lock early, and proto-syntaxes will be annealed while a concave curvature appears (Figures 3, 6, and 8). On the contrary, if the viscosity of the trench is low (< 35 Pa s), the subduction interface is highly lubricated. A more efficient lubrication of the trench allows more continent to subduct, driven by the push of the piston combined with the anchor of the oceanic slab. The slab pull increases continuously, and when it approaches a positive value, the trend reverses and both the curvature and proto-syntaxes are amplified forming an orocline convex toward the south (Figures 4, 5, 7, and 9).

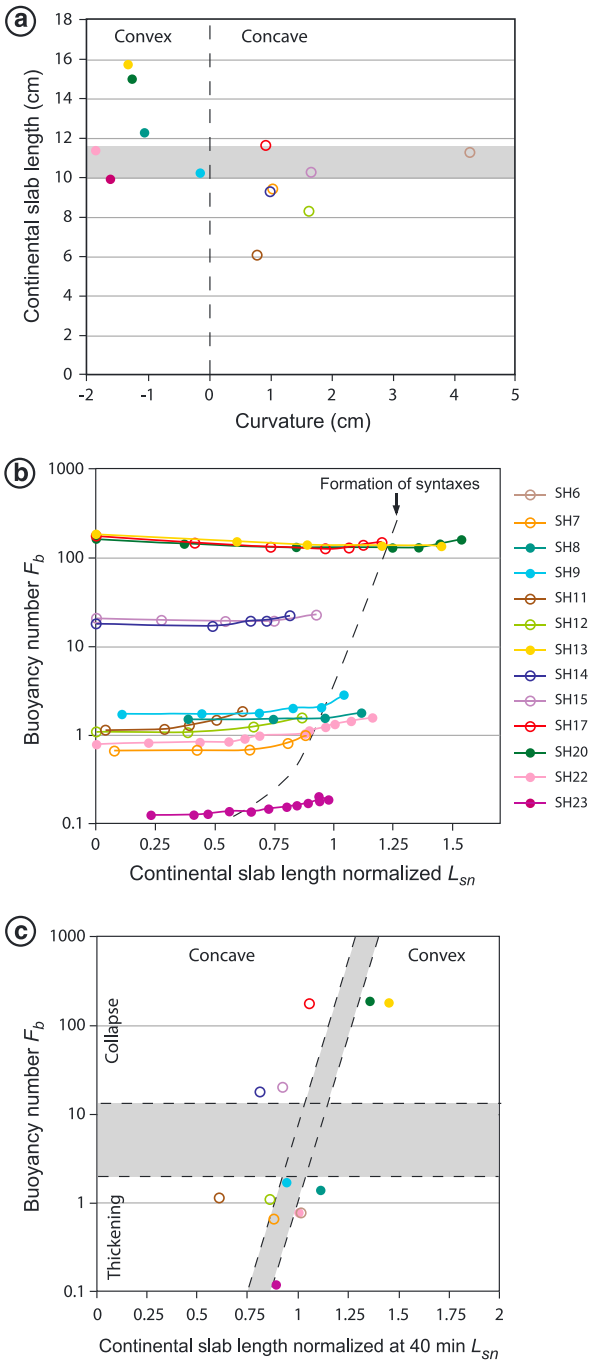

Figure 10. (a) Continental slab length as a function of trench curvature at 40 min (22 My). Filled circles are those of experiments with syntaxes and convex curvature (positive), empty circles those of experiments without syntaxes and concave curvature (negative). The shaded area represents the transition zone between convex and concave oroclines. All experiments with a convex orocline have undergone more than 10 cm of continental subduction (efficient; see text for details). (b) Graph representing the buoyancy number (F_b) versus the normalized continental slab length (L_{sn}). The dotted line highlights the stage of syntaxes formation. (c) Buoyancy number and normalized continental slab length (L_{sn}) at 40 min (22 My) plotted for each experiment showing four domains with concave or convex curvature, and thickening or collapse dynamic. The boundaries between domains are uncertain and illustrated by the shaded area.

The continuity of the subduction process coupled with the positive slab pull generate a convex curvature.

[38] Such shape has been observed when an oceanic plate subducts under its own weight and collapse, generating a toroidal flow that curves the trench toward the subducting plate [*Funiciello et al.*, 2003; *Stegman et al.*, 2010]. Such a flow could not be invoked for a continental subduction, as the trench advances continuously and the mantle flow is directed forward (Figures 3–9).

[39] We can illustrate the effect of subduction efficiency on range shape by plotting the continental slab length (L_s) versus curvature at a certain time (Figure 10a). After 40 min, the experiments showing a convex curvature are those with $L_s > 10 \pm 1$. This efficient subduction is obtained only in experiments with well-lubricated trench. Side-view pictures of these experiments reveal a larger radius of curvature of the subducting plate compared to experiments with concave range (Figures 4c, 5c, 7c, and 9c). Moreover, we observe that the change from straight to convex curvature often occurs when the buoyancy of the slab reaches or is close to neutral value (e.g., Figures 4e and 5e). When this threshold is attained, the slab is no longer pulling down and the subducting plate adopts a larger radius of curvature and underthrusts the upper one at a flat angle. A part of the convergence previously undertaken by the subduction is accommodated by overthrusting of the upper plate on the indenter. The transfer from vertical motion (sinking slab) to horizontal one (relative transversal flow/underthrusting) results in a convex orocline (Figure 11). If the subduction stops, the radius of curvature of the slab is small, and the underthrusting of the subducting plate is reduced. The upper plate does not overthrust the indenter nor curves convexly (Figure 11). More complex shapes can occur when the trench partially locks on one side because of local adhesion of the plates. The trench shape becomes asymmetric, with one convex syntaxis where the subduction is continuous and one concave curve where the trench is locked (Figure 7).

[40] These results are consistent with those of other studies showing the importance of the plates interface in subduction dynamics, especially lubrication [*Luth et al.*, 2010; *Iaffaldano et al.*, 2012]. A strong decoupling at the plate boundary has been shown to lead to underthrusting, while strong coupling reduces subduction efficiency and enhances plate deformation [*Willingshofer and Sokoutis*, 2009].

4.2. Buoyancy Number

[41] The buoyancy number, depending mainly on the thickness and viscosity of the upper plate, is responsible for the amplitude and timing of syntaxes and curvature formation. During convergence, the upper plate undergoes a competition between thickening and collapse. The collapse generates both lateral escape (E-W extrusion) and N-S overthrusting. Syntaxes and convex curvature develop if the relative transversal flow toward the subducting plate is larger at the center of the indenter than on its sides.

[42] The lower the buoyancy number is, the more stable the upper plate is. Three-dimensional strain analysis (Appendix A) performed on a typical experiment (SH9; presented in Figure 5) reveals vertical flattening in the central area of the upper plate, with λ_1 vertical and λ_3 orogen-normal. The most external parts are characterized by plane strain to slight horizontal constriction (Figure 12a). This is coherent with the velocity field showing N-S displacements in the central area and E-W extrusion and

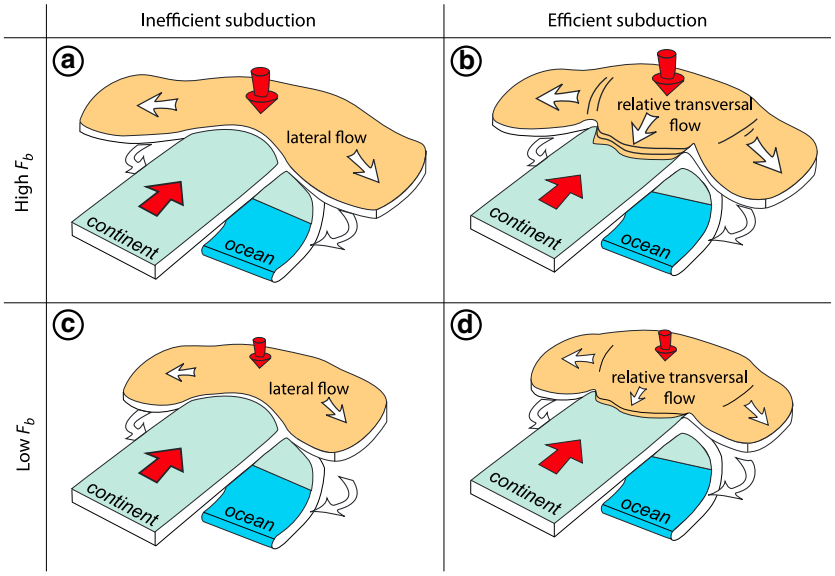

Figure 11. Sketch summarizing the possible indentation dynamics depending on buoyancy number and subduction efficiency. (a) Reduced crustal thickening with indentation, large lateral flow, and no overthrusting; (b) reduced crustal thickening, large lateral flow, and large overthrusting; (c) large crustal thickening with indentation, reduced lateral flow, and no overthrusting; and (d) large crustal thickening, reduced lateral flow, and reduced overthrusting.

rotation in external areas (Figure 5d). In summary, a low F_b (thin and/or strong upper plate) favors the thickening of the upper plate, especially in front of the indenter (Figures 3–5 and 8). Formation of convex curvature and syntaxes is possible if the trench is well lubricated, but amplitude of overthrusting will be small (Figure 11). In that case, both the convex shape of the suture and the thickening of the upper plate are compatible with the Tsangpo suture and thick crust of the Tibetan Plateau.

[43] The higher the buoyancy number is, the more unstable the upper plate is. A high F_b favors gravitational collapse expressed by lateral escape and relative transversal flow (Figures 11 and 12b). The strain in the upper plate is typically that of experiment SH13 (presented in Figure 7) characterized by a λ_1 orogen-parallel and a λ_3 vertical. The central area deforms by horizontal constriction, while external parts undergo horizontal flattening (Figure 12b). This analysis confirms the strong lateral component observed in the velocity field (Figure 7d). To summarize, for a thick and/or low viscosity, upper plate convergence is more accommodated by a very efficient lateral spreading that reduces the amount of thickening and can lead to vertical thinning. A well-lubricated plate interface favors the overthrusting of the upper plate on the

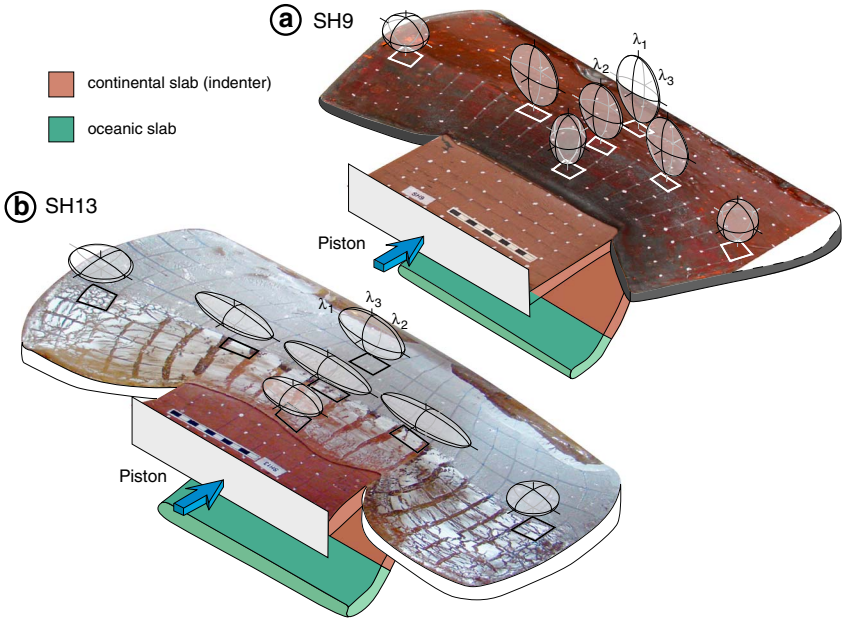

Figure 12. Strain ellipsoids calculated at 40 min (22 My) on two typical experiments (a) SH9 (see Figure 5 for details) and (b) SH13 (see Figure 7 for details). The details of strain analysis are given in Appendix A.

indenter (Figure 11). This dynamic generates a convex curvature and syntaxes of large amplitude compared to experiments with low F_b (e.g., Figures 7, 9, and 11). These results are consistent with thin-viscous-sheet models showing a more important range curvature for upper plates of higher gravitational potential energy [*Copley*, 2012]. However, we also observe that the final shape of the trench is less pronounced for experiment SH9 (Figure 5; $F_b = 1.7$) than for SH22 (Figure 4; $F_b = 0.8$). That can be explained by the temporary stage of concave orocline in SH9 evolution, absent in the case of SH22, that delays the development of convex curvature. The slight difference of viscosity at the plates interface (34.5 Pa s for SH9, 29.5 for SH22) could also account for the lower amplitude of the curvature. In the case of high F_b, the convex shape of the suture is compatible with the Tsangpo suture, but the upper plate is thinning unlike the Tibetan Plateau.

[44] The buoyancy number also influences the timing of syntaxes formation. In all experiments, there is a competition between thickening and lateral escape. High F_b leads to important lateral escape that inhibits thickening and N-S overthrusting compared to low-F_b experiments. Consequently, a larger amount of convergence is required to reach a similar range shape. Figure 10b shows the buoyancy number plotted against the normalized continental slab length. The normalized continental slab length is obtained by dividing the continental slab length (L_s) by the total thickness of glucose syrup in the tank (t_s). The dotted line represents the amount of subduction after which syntaxes form. It is shifted toward larger values for high F_b experiments. In other words, syntaxes and thus convex curvature appear later. To summarize, for low-F_b experiments syntaxes and curvature are of small amplitude and form early in the collision history, while for high F_b experiments they have a larger amplitude and appear later.

4.3. Lateral Decoupling

[45] If the continent is bounded by two lateral oceans (Figures 8 and 9), they subduct vertically or slightly retreat, while the continent moves forward and shapes the range. The parameters controlling the orientation of the suture are identical to experiments without lateral oceans: a low-viscosity trench is required and the buoyancy number influences the amplitude of curvature. However, with lateral oceans the syntaxes are wider and the curvature less pronounced. The extreme lateral decoupling reproduced with a continental indenter alone favors the appearance of an arcuate suture convex toward the upper plate as observed for the Himalayan range (Figure 1). This configuration mimics the strong lateral decoupling of the Indian continent sliding northward along the Sagaing fault to the east and the Chaman fault to the west (Figure 1). It leads to a larger indentation of the upper plate and sharper syntaxes.

4.4. Comparison With the India-Asia Collision

[46] The Himalaya range shape is convex toward the overriding plate, with two syntaxes at both east and west extremities (Figure 1). This shape is correctly reproduced in our experiments, when continental subduction is continuous (Figures 4, 5, 7, and 9). An efficient subduction process seems to be driven by a well-lubricated trench, corresponding to a lower viscosity of the plates interface. When the force balance reaches neutral buoyancy of the slab, the subducting plate underthrusts the upper one at a flat angle, which accommodates a part of the convergence previously undertaken by the subduction. The transfer from a vertical motion (sinking slab) to a horizontal one (relative transversal flow/underthrusting) results in a convex orocline. The global tomography shows that the continental subduction of India has been active since the beginning of the indentation [*Negredo et al*., 2007; *Replumaz et al*., 2010a]. It has been shown that beneath southern Tibet [e.g., *Nabelek et al*., 2009] and Hindu Kush [*Negredo et al*., 2007], this subduction process is coupled with underthursting. The results of our laboratory experiments suggest that this process, active since the beginning of indentation and increasing as collision proceeds, is partly responsible for the curvature of the Himalayan range. This efficient subduction can be explained by the high velocity of the Indian plate due to active convection. This is not the case for other mountain belts showing a curvature concave toward the overriding plate (e.g., Alps and Bitlis) or straight (e.g., Pyrenees and Rocky Mountains). Our results are in disagreement with *Copley et al*. [2011], who conclude that coupling between India and the Tibetan plateau is strong. However, *Copley et al*. [2011] focus on the present-day configuration of the plate margin and do not take into account its subduction/collision history. The mechanism resulting in convex oroclines observed in our experiments is consistent with the results of *Copley* [2012] suggesting that gravitational spreading is a key condition.

[47] The convexity of the Himalayan range observed today and measured in the same way as for our experiments is about 350 km. We have to take into account that we simulated approximately 15 My of collision (occurring generally from 20 to 45 min), while the process began 45 My ago for India-Asia. Our experiments show a linear increase of curvature with time during continental collision, and we can thus extrapolate the value for 45 My. The curvature of experiment SH9 would be equivalent to 310 km after 45 My of collision and the one of SH13 to 400 km. This suggests that the current state of the Himalayan range is best represented by a rheology intermediate between these two experiments.

[48] Experiments with high F_b are dominated by collapse, enhancing the lateral spreading and reducing the thickening in front of the indenter (Figures 6, 7, and 9). The indentation of such a high F_b lithosphere could produce an overall range shape similar to the Himalaya, with a convex curvature (Figures 7 and 9), but could not reproduce the thickening of the Tibetan Plateau and generates an overestimated extrusion. Nevertheless, it may be compared to the late evolution of orogenic plateaux such as Tibet. Indeed, the Tibetan upper plate may become weaker when it thickens [e.g., *Kind et al*., 2002; *Nabelek et al*., 2009], increasing the component of gravitational collapse. The induced lateral spreading would enhance E-W extension activating N-S striking grabens in southern Tibet at approximately 15 My [e.g., *Armijo et al*., 1986; *Williams et al*., 2001] coupled with strike-slip motion along the Jiali fault [*Armijo et al*., 1989]. However, the amount and velocity of collapse of high F_b experiments is probably overestimated compared to the Tibetan Plateau.

5. Conclusions: Four End-Members Regimes of Indentation

[49] Our experiments highlight four end-members regimes of indentation (Figures 10c and 11):

[50] 1. High buoyancy number (collapse), inefficient subduction: collision regime leading to concave curvature and absence of syntaxes, with lateral extrusion as a main process

of deformation of the upper plate and limited thickening (SH15; Figures 6, 10c, and 11a).

[51] 2. High buoyancy number (collapse), efficient subduction: indentation regime enhancing large amplitude syntaxes and convex curvature with large lateral flow, and overthrusting of the upper plate and vertical thinning such as occurring today in the Tibetan plateau (SH13; Figures 7, 10c, and 11b).

[52] 3. Low buoyancy number (thickening) and inefficient subduction: collision regime leading to concave curvature and absence of syntaxes, with thickening coupled to limited lateral extrusion (SH7; Figures 3, 10c, and 11c).

[53] 4. Low buoyancy number (thickening) and efficient subduction: a collisional regime promoting convex curvature and thickening coupled to lateral escape that could be compared to early stages of India-Asia history, and shape of the suture and thickening of the Tibetan Plateau (SH9; Figures 5, 10c, and 11d).

Appendix A: Quantification of Deformation

[54] The grid drawn at the surface of the silicone putties allows us to infer thickness evolution and determine finite strain in various places of the plates. We know the initial dimensions of each square (length L_i, width W_i, and thickness H_i) and are able to measure final length L_f and width W_f after a certain time span from top-view pictures. Assuming isovolume deformation, the final thickness is

$$H_f = (L_i \times W_i \times H_i)/(L_f \times W_f) \quad \text{(A1)}$$

[55] Each length can be measured at ± 0.5 mm, thus giving the final thickness H_f with a precision of ± 10.5%. H_f is used to calculate the thickening factor as detailed in section 2.2. Finite strain is determined at 40 min (equivalent to 22 My) for six squares aligned following a longitudinal and a transversal transect on the upper plate (Figure 10).

[56] We can calculate the principal strains in the direction of convergence (x), lateral escape (y), and vertical (z) such as

$$\lambda_x = (L_f/L_i)^2 \quad \text{(A2)}$$

$$\lambda_y = (W_i/W_f)^2 \quad \text{(A3)}$$

$$\lambda_z = (H_i/H_f)^2 \quad \text{(A4)}$$

[57] Flinn's K parameter defining the aspect ratio of the strain ellipsoids can be expressed as

$$K = (\lambda_1/\lambda_2 - 1)/(\lambda_2/\lambda_3 - 1) \quad \text{(A5)}$$

[58] λ_1, λ_2, and λ_3 being the maximal, intermediate, and minimum principal axes of the strain ellipsoid, respectively. They are represented for two typical experiments (SH9 and SH13) in Figure 12.

Appendix B: Partitioning of the Convergence

[59] The N-S shortening of the upper plate (S_{up}) is calculated as the difference between final and initial lengths (L_{upf} and L_{upi}, respectively)

$$S_{up} = L_{upf} - L_{upi} \quad \text{(B1)}$$

[60] For the shortening of the subducting indenter (S_i), we take into account the length of the continental slab (L_{cs}) such as

$$S_i = L_{if} + L_{cs} - L_{ii} \quad \text{(B2)}$$

Where L_{ii} and L_{if} are the initial and final lengths of the indenter, respectively.

[61] The total shortening due to the piston advance (S_p) is calculated as

$$S_p = v\ t \quad \text{(B3)}$$

Where v is the piston velocity (0.54 cm min^{-1}) and t the time step at which we calculate the partitioning of the convergence (40 min).

[62] The percentage of convergence accommodated by shortening of the upper plate (P_{up}) is

$$P_{up} = 100\ S_{up}/S_p \quad \text{(B4)}$$

[63] The same expression applies for the indenter

$$P_i = 100\ S_i/S_p \quad \text{(B5)}$$

[64] The remaining part of N-S convergence that is not accommodated by shortening of the plates is due to subduction.

[65] **Acknowledgments.** F. Bajolet was funded by the European Union FP7 Marie Curie ITN "Crystal2Plate", contract 215353. Experiments presented in this paper have been realized at the Laboratory of Experimental Tectonics, Università "Roma TRE", Italy. A. Replumaz and R. Lainé were funded by Université de Grenoble Joseph Fourier and LabEx *OSUG@2020*. We are grateful to Syral srl for providing us the sugar syrup used in our experimental models. We are grateful to Claudio Faccenna for stimulating discussions. The paper benefited from constructive reviews by two anonymous referees that helped improve the clarity of the manuscript.

References

Alvarez, W. (2010), Protracted continental collisions argue for continental plates driven by basal traction, *Earth Planet. Sci. Lett.*, *296*(3-4), 434–442, doi:10.1016/j.epsl.2010.05.030.

Armijo, R., P. Tapponnier, and H. Tonglin (1989), Late Cenozoic right-lateral strike-slip faulting in southern Tibet, *J. Geophys. Res.*, *94*(B3), 2787–2838, doi:10.1029/JB094iB03p02787.

Armijo, R., P. Tapponnier, J. L. Mercier, and H. Tong-Lin (1986), Quaternary extension in southern Tibet: Field observations and tectonic implications, *J. Geophys. Res.*, *91*(B14), 13,803–13,872, doi:10.1029/JB091iB14p13803.

Artyushkov, E. V. (1973), Stresses in the lithosphere caused by crustal thickness inhomogeneities, *J. Geophys. Res.*, *78*(32), 7675–7708, doi:10.1029/JB078i032p07675.

Ayoub, F., S. Leprince, and J.-P. Avouac (2009), Co-registration and correlation of aerial photographs for ground deformation measurements, *ISPRS J. Photogramm. Remote Sens.*, *64*(6), 551–560, doi:10.1016/j.isprsjprs.2009.03.005.

Becker, T. W., C. Faccenna, R. J. O'Connell, and D. Giardini (1999), The development of slabs in the upper mantle: Insights from numerical and laboratory experiments, *J. Geophys. Res.*, *104*(B7), 15,207–15,226, doi:10.1029/1999JB900140.

Becker, T. W., and C. Faccenna (2011), Mantle conveyor beneath the Tethyan collisional belt, *Earth Planet. Sci. Lett.*, *310*(3-4), 453–461, doi:10.1016/j.epsl.2011.08.021.

Bellahsen, N., C. Faccenna, F. Funiciello, J. M. Daniel, and L. Jolivet (2003), Why did Arabia separate from Africa? Insights from 3-D laboratory experiments, *Earth Planet. Sci. Lett.*, *216*(3), 365–381, doi:10.1016/s0012-821x(03)00516-8.

Bellahsen, N., C. Faccenna, and F. Funiciello (2005), Dynamics of subduction and plate motion in laboratory experiments: Insights into the "plate tectonics" behavior of the Earth, *J. Geophys. Res.*, *110*, B01401, doi:10.1029/2004JB002999.

Bonnardot, M. A., R. Hassani, and E. Tric (2008), Numerical modelling of lithosphere-asthenosphere interaction in a subduction zone, *Earth Planet. Sci. Lett.*, *272*(3-4), 698–708, doi:10.1016/j.epsl.2008.06.009.

Capitanio, F. A., C. Faccenna, S. Zlotnik, and D. R. Stegman (2011), Subduction dynamics and the origin of Andean orogeny and the Bolivian orocline, *Nature*, *480*(7375), 83–86, doi:10.1038/nature10596.

Chemenda, A. I., J. P. Burg, and M. Mattauer (2000), Evolutionary model of the Himalaya-Tibet system: Geopoem based on new modelling, geological and geophysical data, *Earth Planet. Sci. Lett.*, *174*(3-4), 397–409, doi:10.1016/s0012-821x(99)00277-0.

Conrad, C. P., and B. H. Hager (1999), Effects of plate bending and fault strength at subduction zones on plate dynamics, *J. Geophys. Res.*, *104*(B8), 17,551–17,571, doi:10.1029/1999JB900149.

Copley, A., J.-P. Avouac, and B. P. Wernicke (2011), Evidence for mechanical coupling and strong Indian lower crust beneath southern Tibet, *Nature*, *472*(7341), 79–81, doi:10.1038/nature09926.

Copley, A. (2012), The formation of mountain range curvature by gravitational spreading, *Earth Planet. Sci. Lett.*, *351-352*, 208–214, doi:10.1016/j.epsl.2012.07.036.

Cruden, A. R., M. H. B. Nasseri, and R. Pysklywec (2006), Surface topography and internal strain variation in wide hot orogens from three-dimensional analogue and two-dimensional numerical vice models, *Geol. Soc. Spec. Publ.*, *253*, 79–104.

Davy, P., and P. R. Cobbold (1991), Experiments on shortening of a 4-layer model of the continental lithosphere, *Tectonophysics*, *188*(1-2), 1–25, doi:10.1016/0040-1951(91)90311-F.

De Franco, R., R. Govers, and R. Wortel (2008), Dynamics of continental collision: Influence of the plate contact, *Geophys. J. Int.*, *174*(3), 1101–1120, doi:10.1111/j.1365-246X.2008.03857.x.

Duarte, J. C., W. P. Schellart, and A. R. Cruden (2013), Three-dimensional dynamic laboratory models of subduction with an overriding plate and variable interplate rheology, *Geophys. J. Int.*, *195*(1), 47–66, doi:10.1093/gji/ggt257.

England, P., and D. McKenzie (1982), A thin viscous sheet model for continental deformation, *Geophys. J. R. Astron. Soc.*, *70*(2), 295–321, doi:10.1111/j.1365-246X.1982.tb04969.x.

England, P., and G. Houseman (1986), Finite strain calculations of continental deformation 2. Comparison with the India-Asia collision zone, *J. Geophys. Res.*, *91*(B3), 3664–3676, doi:10.1029/JB091iB03p03664.

Faccenda, M., T. V. Gerya, and S. Chakraborty (2008), Styles of post-subduction collisional orogeny: Influence of convergence velocity, crustal rheology and radiogenic heat production, *Lithos*, *103*(1-2), 257–287, doi:10.1016/j.lithos.2007.09.009.

Funiciello, F., C. Faccenna, D. Giardini, and K. Regenauer-Lieb (2003), Dynamics of retreating slabs: 2. Insights from three-dimensional laboratory experiments, *J. Geophys. Res.*, *108*(B4), 2207, doi:10.1029/2001JB000896.

Funiciello, F., M. Moroni, C. Piromallo, C. Faccenna, A. Cenedese, and H. A. Bui (2006), Mapping mantle flow during retreating subduction: Laboratory models analyzed by feature tracking, *J. Geophys. Res.*, *111*, B03402, doi:10.1029/2005JB003792.

Funiciello, F., C. Faccenna, A. Heuret, S. Lallemand, E. Di Giuseppe, and T. W. Becker (2008), Trench migration, net rotation and slab-mantle coupling, *Earth Planet. Sci. Lett.*, *271*(1-4), 233–240, doi:10.1016/j.epsl.2008.04.006.

Ghosh, A., T. W. Becker, and S. Zhong (2010), Effects of lateral viscosity variations on the geoid, *Geophys. Res. Lett.*, *37*, L01301, doi:10.1029/2009GL040426.

Hetenyi, G., R. Cattin, F. Brunet, L. Bollinger, J. Vergne, J. Nabelek, and M. Diament (2007), Density distribution of the India plate beneath the Tibetan plateau: Geophysical and petrological constraints on the kinetics of lower-crustal eclogitization, *Earth Planet. Sci. Lett.*, *264*(1-2), 226–244, doi:10.1016/j.epst.2007.09.036.

Iaffaldano, G., E. Di Giuseppe, F. Corbi, F. Funiciello, C. Faccenna, and H. P. Bunge (2012), Varying mechanical coupling along the Andean margin: Implications for trench curvature, shortening and topography, *Tectonophysics*, *526*, 16–23, doi:10.1016/j.tecto.2011.09.014.

Kapp, P., and J. H. Guynn (2004), Indian punch rifts Tibet, *Geology*, *32*(11), 993–996, doi:10.1130/g20689.1.

Keep, M. (2000), Models of lithospheric-scale deformation during plate collision: Effects of indentor shape and lithospheric thickness, *Tectonophysics*, *326*(3-4), 203–216, doi:10.1016/s0040-1951(00)00123-2.

Kind, R., et al. (2002), Seismic images of crust and upper mantle beneath Tibet: Evidence for Eurasian plate subduction, *Science*, *298*, 1219–1221.

Lallemand, S., A. Heuret, and D. Boutelier (2005), On the relationships between slab dip, back-arc stress, upper plate absolute motion, and crustal nature in subduction zones, *Geochem. Geophys. Geosyt.*, *6*, Q09006, doi:10.1029/2005GC000917.

Lave, J., and J. P. Avouac (2000), Active folding of fluvial terraces across the Siwaliks Hills, Himalayas of central Nepal, *J. Geophys. Res.*, *105*(B3), 5735–5770, doi:10.1029/1999JB900292.

Leprince, S., F. Ayoub, Y. Klinger, and J.-P. Avouac (2007), Co-Registration of Optically Sensed Images and Correlation (COSI-Corr): An operational methodology for ground deformation measurements, in *Igarss*: *2007 IEEE International Geoscience and Remote Sensing Symposium*, *Vols 1-12*: *Sensing and Understanding Our Planet*, edited, pp. 1943–1946.

Li, C., R. D. Van der Hilst, A. S. Meltzer, and E. R. Engdahl (2008), Subduction of the Indian lithosphere beneath the Tibetan Plateau and Burma, *Earth Planet. Sci. Lett.*, *274*(1-2), 157–168, doi:10.1016/j.epsl.2008.07.016.

Luth, S., E. Willingshofer, D. Sokoutis, and S. Cloetingh (2010), Analogue modelling of continental collision: Influence of plate coupling on mantle lithosphere subduction, crustal deformation and surface topography, *Tectonophysics*, *484*(1-4), 87–102, doi:10.1016/j.tecto.2009.08.043.

Magni, V., J. van Hunen, F. Funiciello, and C. Faccenna (2012), Numerical models of slab migration in continental collision zones, *Solid Earth*, *3*(2), 293–306, doi:10.5194/se-3-293-2012.

Malavieille, J. (1984), Experimental-model for imbricated thrusts - comparison with thrust-belts, *Bull. Soc. Geol. France.*, *26*(1), 129–138.

McCaffrey, R., and J. Nabelek (1998), Role of oblique convergence in the active deformation of the Himalayas and southern Tibet plateau, *Geology*, *26*(8), 691–694, doi:10.1130/0091-7613(1998)026<0691:roocit>2.3.co;2.

Mohadjer, S., et al. (2010), Partitioning of India-Eurasia convergence in the Pamir-Hindu Kush from GPS measurements, *Geophys. Res. Lett.*, *37*, L04305, doi:10.1029/2009GL041737.

Molnar, P., and J. M. Stock (2009), Slowing of India's convergence with Eurasia since 20 Ma and its implications for Tibetan mantle dynamics, *Tectonics*, *28*, TC3001, doi:10.1029/2008TC002271.

Nabelek, J., G. Hetenyi, J. Vergne, S. Sapkota, B. Kafle, M. Jiang, H. P. Su, J. Chen, B. S. Huang, and H.-C. Team (2009), Underplating in the Himalaya-Tibet collision zone revealed by the Hi-CLIMB experiment, *Science*, *325*(5946), 1371–1374.

Negredo, A. M., A. Replumaz, A. Villasenor, and S. Guillot (2007), Modeling the evolution of continental subduction processes in the Pamir-Hindu Kush region, *Earth Planet. Sci. Lett.*, *259*(1-2), 212–225, doi:10.1016/j.epsl.2007.04.043.

Patriat, P., and J. Achache (1984), India Eurasia collision chronology has implications for crustal shortening and driving mechanism of plates, *Nature*, *311*(5987), 615–621, doi:10.1038/311615a0.

Regard, V., C. Faccenna, J. Martinod, O. Bellier, and J. C. Thomas (2003), From subduction to collision: Control of deep processes on the evolution of convergent plate boundary, *J. Geophys. Res.*, *108*(B4), 2208, doi:10.1029/2002JB001943.

Regard, V., C. Faccenna, J. Martinod, and O. Bellier (2005), Slab pull and indentation tectonics: Insights from 3D laboratory experiments, *Phys. Earth Planet. Inter.*, *149*(1-2), 99–113, doi:10.1016/j.pepi.2004.08.011.

Replumaz, A., A. M. Negredo, S. Guillot, and A. Villasenor (2010a), Multiple episodes of continental subduction during India/Asia convergence: Insight from seismic tomography and tectonic reconstruction, *Tectonophysics*, *483*(1-2), 125–134, doi:10.1016/j.tecto.2009.10.007.

Replumaz, A., A. M. Negredo, S. Guillot, P. van der Beek, and A. Villasenor (2010b), Indian continental subduction and slab break-off during Tertiary Collision, *Terra Nova*, *22*(4), 290–296, doi:10.1111/j.1365-3121.2010.00945.x.

Rosenberg, C. L., J. P. Brun, F. Cagnard, and D. Gapais (2007), Oblique indentation in the Eastern Alps: Insights from laboratory experiments, *Tectonics*, *26*, TC2003, doi:10.1029/2006TC001960.

Seeber, L., and A. Pecher (1998), Strain partitioning along the Himalayan arc and the Nanga Parbat antiform, *Geology*, 26(9), 791–794, doi:10.1130/0091-7613(1998)026<0791:spatha>2.3.co;2.

Sokoutis, D., M. Bonini, S. Medvedev, M. Boccaletti, C. J. Talbot, and H. Koyi (2000), Indentation of a continent with a built-in thickness change: Experiment and nature, *Tectonophysics*, *320*(3-4), 243–270, doi:10.1016/s0040-1951(00)00043-3.

Sokoutis, D., and E. Willingshofer (2011), Decoupling during continental collision and intra-plate deformation, *Earth Planet. Sci. Lett.*, *305*(3-4), 435–444, doi:10.1016/j.epsl.2011.03.028.

Stein, S., S. Cloetingh, N. H. Sleep, and R. Wortel (1989), Passive margin earthquake, stress and rheology, in *Earthquakes at the North Atlantic Passive Margin: Neotectonics and Postglacial Rebound*, edited by S. Gregersen and P. W. Basham, pp. 231–259, Kluwer Acad., Norwell, MA.

Stegman, D. R., R. Farrington, F. A. Capitanio, and W. P. Schellart (2010), A regime diagram for subduction styles from 3-D numerical models of free subduction, *Tectonophysics*, *483*(1-2), 29–45, doi:10.1016/j.tecto.2009.08.041.

Tapponnier, P., G. Peltzer, A. Y. Ledain, R. Armijo, and P. Cobbold (1982), Propagating extrusion tectonics in Asia—New insights from simple experiments with plasticine, *Geology*, *10*(12), 611–616, doi:10.1130/0091-7613(1982)10<611:petian>2.0.co;2.

Ton, S., and M. J. R. Wortel (1997), Slab detachment in continental collision zones: An analysis of controlling parameters, *Geophys. Res. Lett.*, *24*(16), 2095–2098.

Turcotte, D. L. (1982), The state of stress at passive continental margin, in *Dynamics of Passive Margins*, Geodyn. Ser., vol. 6, edited by R. A. Scrutton, pp. 141–146, AGU, Washington D. C.

Turcotte, D. L., and G. Schubert (1982), *Geodynamics Application of Continuum Physics to Geological Problems*, John Wiley, New York.

Van der Voo, R., W. Spakman, and H. Bijwaard (1999), Tethyan subducted slabs under India, *Earth Planet. Sci. Lett.*, *171*(1), 7–20, doi:10.1016/s0012-821x(99)00131-4.

van Hinsbergen, D. J. J., B. Steinberger, P. V. Doubrovine, and R. Gassmoeller (2005), Acceleration and deceleration of India-Asia convergence since the Cretaceous: Roles of mantle plumes and continental collision, *J. Geophys. Res.*, *116*, B06101, doi:10.1029/2010JB008051.

Weijermars, R., and H. Schmeling (1986), Scaling of Newtonian and non-Newtonian fluid dynamics without inertia for quantitative modeling of rock flow due to gravity (including the concept of rheological similarity), *Phys. Earth Planet. Inter.*, *43*, 316–330, doi:10.1016/0031-9201(86)90021-X.

Weijermars, R. (1986), Flow behavior and physical-chemistry of bouncing putties and related polymers in view of tectonic laboratory applications, *Tectonophysics*, *124*(3-4), 325–358, doi:10.1016/0040-1951(86)90208-8.

Williams, H., S. Turner, S. Kelley, and N. Harris (2001), Age and composition of dikes in southern Tibet: New constraints on the timing of east-west extension and its relationship to postcollisional volcanism, *Geology*, *29*(4), 339–342, doi:10.1130/0091-7613(2001)029<0339:AACODI>2.0.CO;2.

Willingshofer, E., and D. Sokoutis (2009), Decoupling along plate boundaries: Key variable controlling the mode of deformation and the geometry of collisional mountain belts, *Geology*, *37*(1), 39–42, doi:10.1130/g25321a.1.

Wortel, M. J. R., and W. Spakman (2000), Geophysics—Subduction and slab detachment in the Mediterranean-Carpathian region, *Science*, *290*(5498), 1910–1917, doi:10.1126/science.290.5498.1910.

Zhong, S. J., and M. Gurnis (1994), Controls on trench topography from dynamic-models of subducted slabs, *J. Geophys. Res.*, *99*(B8), 15,683–15,695.